

Photovoltaic blend microstructure for high efficiency post-fullerene solar cells. To tilt or not to tilt?

Gang Wang^{a, ‡}, Steven M. Swick^{a, ‡}, Micaela Matta^{a, ‡}, Subhrangsu Mukherjee^b, Joseph W. Strzalka^c, Jenna Leigh Logsdon^a, Simone Fabiano^d, Wei Huang^a, Thomas J. Aldrich^a, Tony Yang^a, Amod Timalisina^a, Natalia Powers-Riggs^a, Joaquin Alzola^a, Ryan M. Young^a, Dean M. DeLongchamp^{b,*}, Michael R. Wasielewski^{a,e,*}, Kevin L. Kohlstedt^{a,*}, George C. Schatz^{a,*}, Ferdinand S. Melkonyan^{a,*}, Antonio Facchetti^{a,f,*}, Tobin J. Marks^{a,*}

^a Department of Chemistry, the Center for Light Energy Activated Redox Processes (LEAP), and the Materials Research Center, Northwestern University, 2145 Sheridan Road, Evanston, Illinois 60208, United States

^b Material Science and Engineering Division, National Institute of Standards and Technology, Gaithersburg, Maryland 20899, United States

^c X-Ray Science Division, Argonne National Laboratory, Argonne, IL 60439, United States

^d Laboratory of Organic Electronics, Department of Science and Technology, Linköping University, SE-60174 Norrköping, Sweden

^e Department of Chemistry and Institute for Sustainability and Energy at Northwestern, Northwestern University, Evanston, IL 60208-3113, United States

^f Flexterra Corporation, 8025 Lamon Avenue, Skokie, Illinois 60077, United States

KEYWORDS: *post-fullerene solar cells; donor-acceptor heterojunction morphology; molecular dynamics computation; domain purity; polymer aggregation; high efficiency*

ABSTRACT: Achieving efficient polymer solar cells (PSCs) requires a structurally optimal donor-acceptor heterojunction morphology. Here we report the combined experimental and theoretical characterization of a benzodithiophene-benzothiadiazole donor polymer series (PBTZF4-R; R = alkyl substituent) blended with the non-fullerene acceptor ITIC-Th, and analyse the effects of substituent dimensions on blend morphology, charge transport, carrier dynamics, and PSC metrics. Varying substituent dimensions has a pronounced effect on the blend morphology with a direct link between domain purity, to some extent domain dimensions, and charge generation and collection. The polymer with the smallest alkyl substituent yields the highest PSC power conversion efficiency (PCE, 11%), reflecting relatively small, high-purity domains, and possibly benefiting from “matched” donor polymer - small molecule acceptor orientations. The distinctive morphologies arising from the substituents are investigated using molecular dynamics (MD) computation which reveals that substituent dimensions dictate a well-defined set of polymer conformations, in turn driving chain aggregation, and ultimately, the various film morphologies and mixing with acceptor small molecules. A straightforward energetic parameter explains the experimental polymer domain morphological trends, hence PCE, and suggests strategies for substituent selection to optimize PSC materials morphologies.

INTRODUCTION

Photovoltaic devices based on organic semiconductors represent a promising, scalable, light-weight, and inexpensive solution for solar energy conversion.¹⁻³ Presently, the most efficient polymer solar cells (PSCs) are based on bulk heterojunction (BHJ) active layer architectures utilizing a p-type, electron-donating material (typically a polymer) and an n-type, electron-accepting material (typically a small molecule) to form networks of semiconducting domains. Irrespective of the semiconductors employed, polymer donor:acceptor interpenetrating microstructures with domains of proper sizes and purity

are essential for efficient BHJ PSCs.⁴ Films with insufficient donor-acceptor phase separation cannot efficiently transport photogenerated charges to the electrodes, while too large phase separation length scales inhibit exciton dissociation and enhance charge recombination, all factors compromising PSC short-circuit current density (J_{sc}) and fill-factor (FF), and thus power conversion efficiency (PCE).⁴⁻¹²

Given the importance of BHJ morphology on PSC performance, there has been extensive research on optimizing active layer morphology,^{4, 5, 13, 14} with polymer substituent (side chain) engineering proving an effective,¹⁵⁻¹⁹ albeit labour-intensive

strategy. Unfortunately however, because of the idiosyncratic nature of polymers and molecular materials in general, the optimal length and shape of polymer substituents (known to impact film morphology)^{10, 20, 21} is usually determined empirically, reflecting limited atomistic understanding of how substituent lengths and shapes affect polymer conformations, how these conformational states govern intermolecular interactions, and how these intermolecular interactions shape the resulting BHJ morphology. A theoretical relationship between the nature of the polymer substituent and its conformation for a given backbone would be a valuable predictive tool for designing and realizing optimal next-generation PSC BHJ morphologies.²²⁻²⁴

Here we report a combined experimental and computational study of a tetrafluorinated benzodithiophene(BDT-R)-benzothiadiazole(BT) based copolymer family, **PBTZF4-R**, featuring a BDT backbone substituted with alkyl R substituents of varying dimensions (Fig. 1a). It will be seen that the polymer with the shortest 2-ethylhexyl substituent (**PBTZF4-EH**, R = 2-EH) achieves a very good PCE of 11.01 % in blends with the acceptor **ITIC-Th**, whereas polymers featuring longer 2-butyloctyl (**PBTZF4-BO**, R = 2-BO), 2-hexyldecyl (**PBTZF4-HD**, R = 2-HD), and 2-octyldecyl (**PBTZF4-OD**, R = 2-OD) side chains exhibit a downward trend in J_{SC} and PCE (9.27 %, 6.06 %, 2.79 %, respectively) when blended with the same acceptor. Paracrystalline g-factor calculations and pole figure analysis are performed to further quantify the morphology, revealing that the **PBTZF4-EH** neat and blend films have greater crystallinity, and that π -face-on and π -edge-on oriented domains (with respect to the electrode plane) co-exist. Detailed microstructural characterisation with resonant soft x-ray scattering (R-SoXS)

and charge generation rate measurements, show that the domain purity, and to a lesser extent domain size, is: 1) correlated with the alkyl substituent length, 2) is a major factor governing charge generation and collection, and consequently FF , J_{SC} , 3) likely surpasses π -face-on/ π -edge-on orientation effects in determining PSC performance (hence the title, “To Tilt or not to Tilt?”). To build a detailed, semiquantitative model explaining the correlation between alkyl substituent length, domain purity, and domain size, molecular dynamics (MD) calculations are performed on isolated polymer chains to accurately determine the accessible backbone conformations. Through careful analysis of these results, we extract a rational design parameter from the computed polymer conformations that correlates well with the film microstructure metrics that ultimately dictate PSC performance.

RESULTS

Donor polymer synthesis and characterisation

The **PBTZF4-R** series was synthesised by Stille polycondensation of the fluorinated, alkyl-substituted building block 4,8-bis(thiophene-2-yl)-benzo [1,2-b:4,5-b']dithiophene (BDT-R) with the fluorinated building block 4,7-dithien-2-yl-2,1,3-benzothiadiazole (BT) (Fig. 1).²⁵ For simplicity, we refer to **PBTZF4-EH** as **P-EH**, **PBTZF4-BO** as **P-BO**, **PBTZF4-HD** as **P-HD**, and **PBTZF4-OD** as **P-OD**. See Supplementary for details on BDT-R and BT building block syntheses. The donor polymer **PBTZF4-H** (**P-H**, R = *n*-hexyl) with *n*-hexyl substituents was also synthesised. However, due to poor processability/solubility, films fabricated using **PBTZF4-H** were of low quality and the

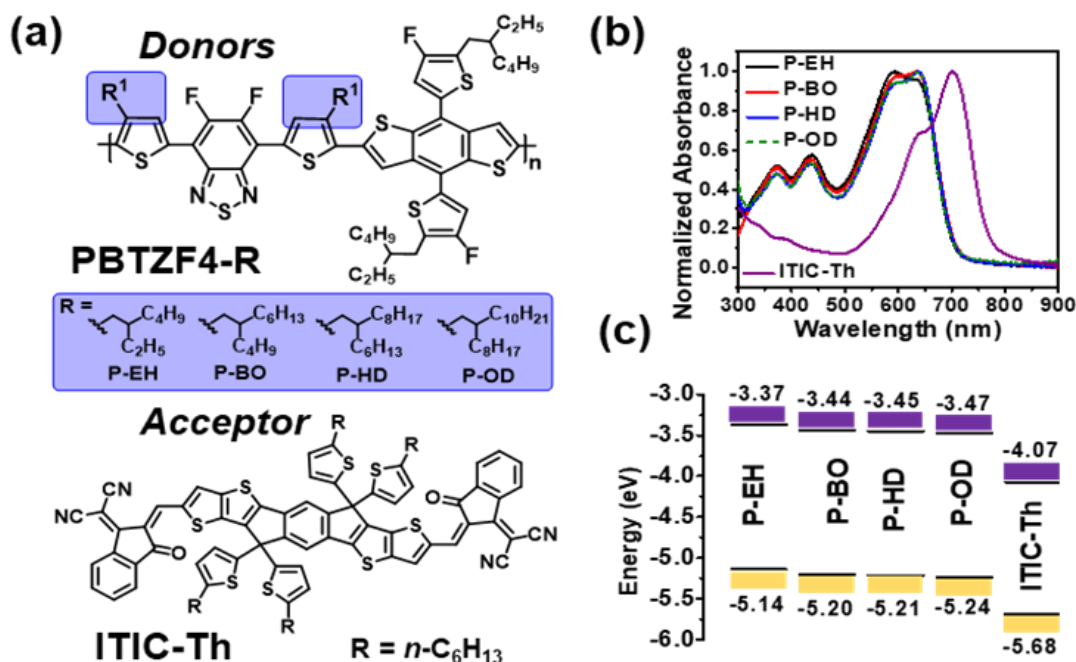


Figure 1. Donor and acceptor materials and their physicochemical properties. a) P-EH, P-BO, P-HD, P-OD and ITIC-Th molecular structures; b) Film optical absorption spectra of P-EH, P-BO, P-HD, P-OD, and ITIC-Th. Neat films of the polymer were spin-coated from PhCl solutions (5 mg mL⁻¹) and neat ITIC-Th films were spin-coated from CHCl₃ solutions (5 mg mL⁻¹); c) Energy level diagrams for P-EH, P-BO, P-HD, P-OD, and ITIC-Th.

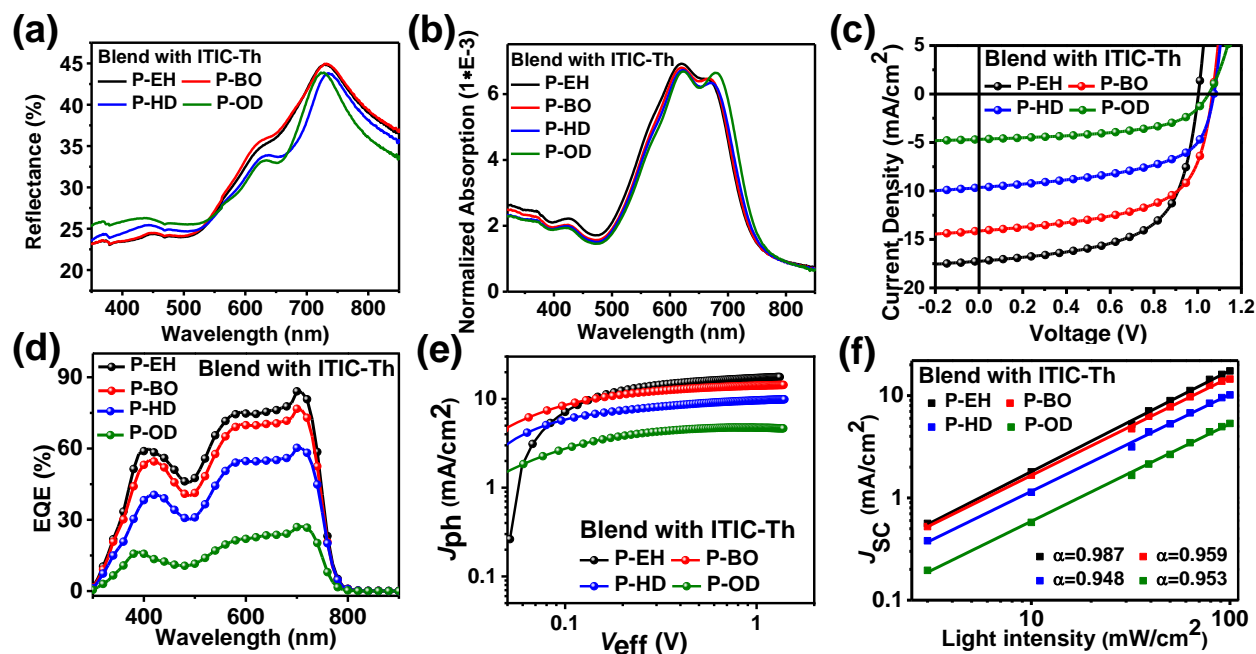


Figure 2. PBTZF4-R:ITIC-Th blends photophysics, photovoltaic and charge transport properties. **a)** reflectance spectra, **b)** thickness normalized absorption spectra, **c)** J - V plots under AM 1.5 G illumination, **d)** External quantum efficiency (EQE) spectra, **e)** J_{ph} dependence on V_{eff} , **f)** J_{sc} dependence on light intensity (I).

resulting PSCs exhibit negligible PCE ($\approx 0.05\%$). PBTZF4-R physical, optical, and electrochemical properties are summarised in Supplementary Table 1 and Supplementary Figs. 1-6. All polymer films exhibit similar optical absorption features (Fig. 1b) with an absorption onset (λ_{onset}) of ≈ 705 nm, corresponding to optical bandgaps of ≈ 1.76 eV. Ultraviolet photoelectron spectroscopy (UPS) was used to characterise the polymer highest occupied molecular orbital (HOMO) energies for P-EH, P-BO, P-HD, and P-OD, which are -5.14, -5.20, -5.21, and -5.24 eV, respectively (Fig. 1c). The polymers also exhibit similar lowest unoccupied molecular orbital (LUMO) energy levels, which were calculated by adding the optical bandgap to the UPS derived HOMO. The HOMO and LUMO values for ITIC-Th were estimated using cyclic voltammetry and showed favourable alignment with the polymers.

The PBTZF4-R polymers were characterised by high-temperature gel permeation chromatography (GPC) and differential scanning calorimetry (DSC). GPC reveals that increasing the R dimensions from 2-ethylhexyl to 2-butyloctyl correlates with increased number average molecule weight (M_n) from 17.9 kg/mol to 33.0 kg/mol, likely reflecting solubility effects in the catalytic polymerisation, although additional R lengthening does not increase M_n further. DSC shows an inverse correlation between R length and both melting temperature and heat of fusion. Thus P-BO, P-HD, and P-OD have melting temperatures of 340.2 °C, 328.3 °C, and 301.7 °C, respectively. This trend indicates that polymer intermolecular interactions decrease with larger alkyl substituents.²⁶ Interestingly, P-EH does not exhibit detectable phase transitions below the decomposition temperature as indicated by tandem TGA/DSC measurements (Supplementary Fig. 6), likely reflecting the strong polymer interchain interactions (*vide infra*).

Photophysics and charge transport

Photovoltaic Response. PBTZF4-R photovoltaic performance was characterised in inverted architecture PSCs of the structure ITO/ZnO/Active Layer/MoO_x/Ag using ITIC-Th as the acceptor. All the blend films exhibit complementary light absorption when blended with ITIC-Th, evident in the optical absorption spectra (Fig. 2b). In order to estimate differences in device reflectance at the active layer interfaces, reflectance measurements of the blend films were performed using an integrating sphere (experimental details: Methods Section, page S2), revealing similar reflectance (variations $<5\%$) between all the films (Fig. 2a). In addition, thin film absorption measurements were performed using an integrating sphere to account for differences in optical absorption and light scattering of the blends (experimental details: Methods Section, page S2). From the film thickness normalized absorption spectra, it can be clearly seen that the absorption between the blends is very similar (Fig. 2b). Given the similar active layer thickness of the devices (100 nm), it can be concluded that differences in absorption between the different blends plays a minor role in device performance and does not account for the 4-fold change in J_{sc} (4.57 to 17.35 mA/cm²) observed across the polymer series (*vide infra*).

Representative current density-voltage (J - V) plots are provided in Fig. 2c, and Table 1 summarises the performance metrics. By increasing the R length in PBTZF4-R from EH to OD, the J_{sc} decreases steadily from 17.35 to 4.57 mA/cm². Interestingly, the decrease in J_{sc} shows a general correlation with an increasing proportion of face-on domains vs edge on domains (*vide infra*). However, the ratio of face-on vs edge-on domains in the P-BO and P-HD blends is identical, but a large difference in J_{sc} (>3 mA/cm²) is observed between the two, indicating that the orientational order of the polymers is not likely a major performance factor here. The FF also tracks the R length, with the P-

Table 1. Photovoltaic and SCLC device parameters for PBTZF4-R:ITIC-Th blends^a

Donor	V_{oc} (V)	J_{sc} (mA/cm ²)	FF (%)	PCE (%)	μ_h	μ_e	μ_h/μ_e
P-EH	1.00±0.01	17.35±0.85	62.05±2.35	10.75±0.26 (11.01)	1.20±0.46	1.01±0.25	1.19
P-BO	1.07±0.01	14.12±0.66	61.39±2.20	9.27±0.28 (9.55)	1.25±0.43	6.31±1.32	0.20
P-HD	1.07±0.02	9.90±0.76	57.21±2.55	6.06±0.35 (6.41)	2.88±0.34	1.20±0.66	2.40
P-OD	1.06±0.01	4.57±0.35	57.49±2.65	2.79±0.12 (2.91)	3.80±0.59	3.98±0.70	0.95

^a) Donor:Acceptor mass ratio = 1:1.2; values are the average of 8 devices; PCE in parentheses is the largest value; μ_h and μ_e given in $10^4 \times$ (cm²/V s).

EH, P-BO, P-HD, and P-OD blend FFs falling, with values of 62%, 61%, 57%, and 57%, respectively. It will be seen that these data correlate well with the domain purity and bimolecular recombination efficiency - the higher FFs paralleling greater purity and lower levels of bimolecular recombination (*vide infra*).²⁷ Note however that the open circuit voltages (V_{oc} s), which depend largely on the LUMO and HOMO energies, show minimal R dependence, with values ranging from ≈ 1.00 V to 1.07 V. The blend external quantum efficiency (EQE) spectra (Fig. 2d) all exhibit similar broad photoresponses from 300 nm to 780 nm, but with photoresponse magnitudes that inversely track with substituent length. Taken together, the large uniform decrease across the EQE spectrum with increasing R length suggests that the formation of excessively large and impure domains may be factors limiting charge generation, as discussed below.^{6,7}

Charge Transport. To probe the vertical charge transport in the **PBTZF4-R:ITIC-Th** blends, single carrier space-charge-limited current (SCLC) diodes of the structure ITO/ZnO/Active layer/LiF/Al (electron-only) and ITO/MoO_x/Active layer/MoO_x/Ag (hole-only) were fabricated and evaluated (Table 1 and Supplementary Fig. 7). Excluding the **P-EH:ITIC-Th** blends, hole mobilities (μ_h) in **PBTZF4-R:ITIC-Th** blends exhibit a strong, positive correlation with polymer face-on domain size (estimated using q_{xy} (100), correlation lengths (CLs) = 4.3 nm to 5.4 nm, Supplementary Fig. S8, Supplementary Table 3). For the **P-EH:ITIC-Th** films, although having large face-on polymer domain sizes (q_{xy} (100) CL = 6.6 nm), the relatively low μ_h may reflect the presence of large edge-on polymer domains (q_z (100) CL = 11.4 nm), which are not present in other blends, providing a less direct hole extraction pathway.²⁷ This correlation of μ_h with the domain orientation of the polymers is also borne out to some extent in the overall ratio of face-on vs edge-on domains (pole figure analysis, *vide infra*), which shows a general correlation between the face-on vs edge-on ratio with μ_h across the entire series of polymers. However, in the case of the **P-BO** and **P-HD** blends, the proportion of face-on vs edge-on domains is unchanged, but a 2-fold increase in the **P-HD** blend μ_h is observed. This indicates that the μ_h is more strongly governed by the domain size (q_{xy} (100) CLs = 4.3 nm vs 4.8 nm) or other confounding factors, rather than overall orientational distribution of the polymers. The electron mobilities (μ_e) appear to follow a similar trend, with larger **ITIC-Th** π -face-on domain sizes (estimated from q_z (010) CLs) correlating with larger μ_e s (Supplementary Fig. S8) and larger **ITIC-Th** π -edge-

on domains (estimated from q_{xy} (010) CLs) correlating with smaller μ_e s (Supplementary Fig. S8), suggesting that the overall blend mobilities are least partly influenced by the π -face-on to edge-on domain size ratios. Interestingly, the highest performing **P-EH:ITIC-Th** blend exhibits the smallest μ_h and μ_e , whereas the lowest performing **P-OD:ITIC-Th** blend has μ_h s and μ_e s $\sim 4\times$ larger, with both blends exhibiting balanced mobilities (important in suppressing space-charge build up),²⁸ indicating that charge mobility is not the determining factor governing device performance in these systems where morphology differs so greatly among blends (*vide infra*). Note that device models,^{29,30} while providing an intuitive description of charge generation and transport, have consistently undervalued film morphological details. Recent efforts to either use genetic algorithms to predict morphology or direct parametrization of film micrographs have only begun to incorporate molecular details into these models.³¹

Charge generation and recombination. Light intensity (I_{light}) dependent photocurrent measurements on the **PBTZF4-R:ITIC-Th** blends were next carried out to investigate charge carrier recombination (Fig. 2f).^{32,33} Importantly, the slope of the J_{sc} vs. I_{light} curve, α , is closest to unity for the **P-EH:ITIC-Th** blend ($\alpha = 0.99$), and larger than those of the other blends (0.95 to 0.96) indicating that the **P-EH:ITIC-Th** has the lowest level of bimolecular recombination. The enhanced bimolecular recombination in **P-HD** and **P-OD** blends can be attributed to the lower domain purity (*vide infra*), and in **P-BO** and **P-HD**, imbalanced film carrier mobilities may also play a role. In addition, photocurrent density (J_{ph}) vs. effective applied voltage (V_{eff}) measurements were made to probe the blend charge generation rates (Fig. 2e). Here, J_{ph} is defined as $J_L - J_D$ where J_L and J_D are the current densities under 1.0 sun illumination and in the dark, respectively. V_{eff} is defined as $V_0 - V_a$ where V_0 is the voltage at which $J_{ph} = 0$ and V_a is the applied bias. It is generally assumed that all the photogenerated charges are dissociated into free charge carriers at high V_{eff} , thus the maximum charge generation rate (G_{max}) will determine the greatest saturation current density (J_{sat}). Note that J_{ph} reaches a J_{sat} of 17.89 mA/cm² for **P-EH** and decreases steadily with increasing substituent length to 4.78 mA/cm² for **P-OD**. This trend in decreasing J_{sat} correlates well with domain purity and to some extent, domain size (*vide infra*), with lower domain purity and larger domain size correlating with smaller J_{sat} s due to enhanced recombination and intrinsic limits in charge diffusion lengths.

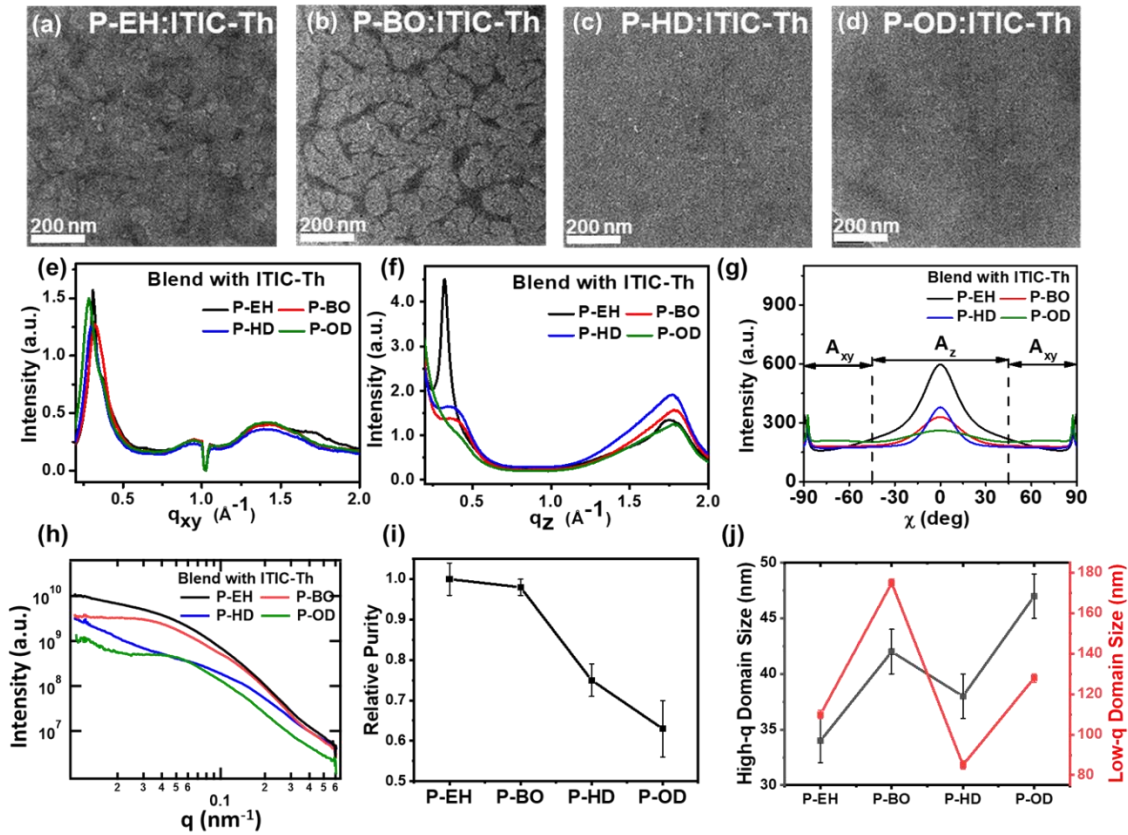


Figure 3. Morphology and microstructure of PBTZF4-R:ITIC-Th blend films, a-d) BF-TEM images, e, f) in-plane (q_{xy}) and out-of-plane (q_z) linecuts of 2D GIWAXS, and g) Pole figures extracted from the lamellar diffraction, Definitions of the polar angle (χ) range corresponding to the edge-on (A_z) and face-on (A_{xy}) crystallites are shown. h) R-SoXS profiles at high material contrast (284 eV), i) R-SoXS domain purity summary, j) R-SoXS domain size summary. Purity and size error bars in (i) and (j) are standard deviation of respective values calculated from R-SoXS data at multiple energies in the range of 283 to 284 eV.

Similarly, using the relationship $J_{\text{sat}} = qLG_{\text{max}}$ where q is the elementary charge and L is the active layer thickness, note that the **P-EH** blend exhibits the greatest G_{max} of $1.12 \times 10^{28} \text{ m}^{-3}\text{s}^{-1}$ with **P-BO**, **P-HD**, and **P-OD** exhibiting G_{max} values of $8.81 \times 10^{27} \text{ m}^{-3}\text{s}^{-1}$, $6.14 \times 10^{27} \text{ m}^{-3}\text{s}^{-1}$, and $2.99 \times 10^{27} \text{ m}^{-3}\text{s}^{-1}$, respectively.

Taken together, these results indicate that the greatest J_{sc} exhibited by the **P-EH:ITIC-Th** blend can be attributed to a greater charge generation rate and lower rates of recombination, stemming largely from morphology differences (*vide infra*). Furthermore, femtosecond transient absorption spectroscopy (fsTA, Supplementary Figs.18-24) data show negligible differences in the charge transfer times (all < 5 ps) and in the decays of each blend. This result suggests that, unlike other systems,³⁴ the present blend performance displays a strong dependence on the π -materials packing, not easily discernible by fsTA outside the conditions of a functioning device.

Microstructure analysis

Transmission Electron Microscopy. Bright-field Transmission electron microscopy (BF-TEM) was used to probe the **PBTZF4-R:ITIC-Th** blend surface and bulk morphological features. BF-TEM samples were prepared with the same film thickness under conditions identical to device fabrication. BF-TEM images of **P-EH:ITIC-Th** and **P-BO:ITIC-Th** blends (Figs. 3a and 3b) show higher contrast than the BF-TEM images of **P-HD:ITIC-Th** and **P-OD:ITIC-Th** (Figs. 3c and 3d), suggesting differences in phase

separation and domain purity. For this reason we next analysed the purities and length scales of the blends using resonant soft x-ray scattering (R-SoXS, *vide infra*).

Grazing Incidence Wide Angle X-ray Scattering (GIWAXS). The textures of the neat donor polymer and **ITIC-Th** films were analysed by GIWAXS. The corresponding q_z (out-of-plane) and q_{xy} (in-plane) linecuts, together with a data summary are provided in Supplementary Figures 11-12 and Supplementary Table 2. For all **PBTZF4-R** films, a lamellar stacking peak is observed in the q_{xy} direction suggesting a π -face-on polymer domain orientation relative to the substrate plane. Furthermore, all polymers exhibit a (010) π - π stacking peak in the q_z direction, further corroborating a π -face-on orientation. Interestingly, unlike the other polymers, **P-EH** also exhibits a strong lamellar reflection in the q_z direction ($d_{100} = 19.11 \text{ \AA}$, $CL = 63.73 \text{ \AA}$), implying the presence of π -edge-on domains as well.^{35, 36} Similarly, diffraction patterns from neat **ITIC-Th** films evidence both π -face-on and π -edge-on domains from the presence of q_z (010) and (100) reflections and q_{xy} (010) and (100) reflections.^{37, 38} Thus, neat **P-BO**, **P-HD**, and **P-OD** films have primarily π -face-on oriented domains, whereas **P-EH** and **ITIC-Th** clearly exhibit both π -face-on and π -edge-on domains.

Next, the **PBTZF4-R:ITIC-Th** blends were examined by GIWAXS; 2D patterns and the corresponding linecuts are

shown in Figs. 3e and 3f and Supplementary Fig. 13, while relevant data are summarised in Supplementary Table 3. All blends exhibit strong lamellar peaks located at $\sim 0.27 \text{ \AA}^{-1} - 0.31 \text{ \AA}^{-1}$ in the q_{xy} direction assignable to the donor polymer, suggesting an edge-on alkyl-chain stacking and potentially corresponding to π -face-on backbone orientation relative to the substrate surface.⁴¹⁻⁴³ Reflections located at $q_z \sim 1.76 \text{ \AA}^{-1} - 1.80 \text{ \AA}^{-1}$, present in all blends, are assignable to donor polymer π - π stacking ($d_{010} = 3.49 \text{ \AA} - 3.58 \text{ \AA}$) and are consistent with polymer domain π -face-on orientation. In addition to the lamellar reflection in the q_{xy} direction, the **P-EH:ITIC-Th** blend exhibits a very strong reflection in the q_z direction ($d_{100} = 19.36 \text{ \AA}$, CL = 114.01 \AA) indicating the presence of both π -edge-on domains as well, as in the neat polymer. In addition to polymer reflections, **ITIC-Th** reflections are observed as well. In all blends, **ITIC-Th** reflections at $q_{xy} \sim 0.33 \text{ \AA}^{-1}$ to 0.44 \AA^{-1} ($d_{100} = 14.30 \text{ \AA}$ to 19.14 \AA) and $q_z \sim 1.47 \text{ \AA}^{-1}$ ($d_{010} \sim 4.2 \text{ \AA}$) are present and indicate the presence of π -face-on domains.³⁹ In addition, peaks located at $q_{xy} = 1.36 \text{ \AA}^{-1}$ to 1.45 \AA^{-1} ($d_{010} = 4.34 \text{ \AA}$ to 4.63 \AA) and at $q_z = 0.353 \text{ \AA}^{-1}$ to 0.421 \AA^{-1} ($d_{100} = 14.92 \text{ \AA}$ to 17.80 \AA) can also be attributed to **ITIC-Th** and indicate the presence of π -edge-on domains.

To gain deeper insight into structural orientation, a blend film pole figure analysis was also performed. The pole figures extracted from the alkyl (100) reflection of the four kinds of blend films are shown in Fig. 3g. See Supplementary Fig. 15 for details on the neat films. The areas integrated with polar angle χ ranges of (-90°) to (-45°) and 45° to 90° (A_{xy}) and (-45°) to 45° (A_z) correspond to the fractions of π -face-on and π -edge-on domains extracted from the (100) peak intensity, respectively.⁴⁰ Using this definition, the ratio of π -edge-on to π -face-on domains is calculated. All results are obtained by integrating a fit of a sum of pseudo-Voigt functions plus a constant (isotropic) term to the pole figures constructed from the 2D-GIWAXS data. For all four blend films, the isotropic term contributes most of the intensity suggesting the intensity-weighted mean orientation is close to that expected for an isotropic distribution. The resulting values A_{xy}/A_z (Supplementary Table 5) show that for the neat films, only **P-EH** and **ITIC-Th** have a ratio < 1 , indicating a greater proportion of π -edge-on domains vs π -face-on domains, whereas in neat **P-BO**, **P-HD**, and **P-OD** films the domains are primarily oriented π -face-on. In all of the blend films, the ratio $A_{xy}/A_z < 1$, which indicates a greater proportion of π -edge-on domains vs π -face-on domains. Among them, **P-EH** has the lowest A_{xy}/A_z and thus the greatest proportion of π -edge-on domains and **P-OD** contains the smallest proportion of π -edge-on domains. In addition, we cannot compare the orientation distributions simply to the A_{xy}/A_z values of previous reports,⁴⁵ as they do not appear to have fit the data to eliminate background contributions to the pole figure, nor do they specify whether they have computed A_{xy}/A_z using the sine-weighted pole figure data as done here. Finally, the **P-EH** blend film pole figures (Fig. 3g and Supplementary Fig. 16.2) appear to be a linear combinations of the neat **ITIC-Th** and **P-EH** pole figures, suggesting that the morphology of each component is maintained in the blend, while in the other blends the morphology is disrupted, consistent with the greater crystallinity from the g -factor estimations (*vide infra*), and stronger intermolecular forces inferred from

MD simulations (*vide infra*) and melting points (*vide supra*). Furthermore, because of the morphology of each component is maintained in the blend, the similar A_{xy}/A_z values of neat **ITIC-Th** and **P-EH** (0.69 for **P-EH** vs 0.53 for **ITIC-Th**), implies a “matched” orientation between the components in the blend, which may contribute to the observed enhanced charge generation.⁴¹ The vertical composition was also considered as a factor influencing device properties.¹³ From the depth profiling results (Supplementary Fig. 17) the vertical phase distributions are almost identical for all blend films. Thus, the effects of vertical phase distributions on PSC metrics should be minor.

Paracrystallinity and g -factor Analysis. Since the present donor polymers are highly disordered, a film paracrystallinity g -factor analysis (See Methods, Supplementary, and Supplementary Table 4) was performed to estimate the degree of crystallinity using the narrow alkyl-stacking diffraction peak. The g -factor is 10.9 % for the **P-EH** blend film, while it is 21.5 %, 22.4 %, and 22.6 % for the **P-BO**, **P-HD**, and **P-OD** blend films. From previous studies,⁴² film g -factors larger than $\sim 10\%$ are regarded as having amorphous texture. Thus, the **P-EH** blend films can be regarded as partially paracrystalline, while the other three blend films can be regarded as strictly amorphous.

Resonant Soft X-ray Scattering. R-SoXS profiles acquired at a high material contrast energy (284 eV) are shown in Fig. 3h. The profile shapes for the four blend samples are found to be similar with two distinct features in the q -ranges $0.04 \text{ nm}^{-1} - 0.06 \text{ nm}^{-1}$ and $0.1 \text{ nm}^{-1} - 0.2 \text{ nm}^{-1}$. Integration of the scattering profiles reveals that the relative domain purity (averaged over all size scales), which is proportional to the square root of the integrated scattering intensity (ISI), of the donor polymer blends decreases with increasing alkyl chain length as shown in Fig. 3i. This trend is in agreement with the **FF** and **bimolecular** recombination rates, with **P-EH** and **P-BO** exhibiting higher domain purity and **FF**, and lower levels of **bimolecular recombination** than **P-HD** and **P-OD** (*vide supra*).^{8,9,27} In addition, size scales corresponding to low- q and high- q features in the R-SoXS profiles were extracted (**R-SoXS analysis section, Page S5-S7 in Supplementary Information**). Although the trend in domain size (Fig. 3j) is less straightforward than that of the domain purity, useful information was extracted. Compared to **P-EH**, **P-BO** exhibits substantially larger domains (**P-EH**: 34 nm and 110 nm, **P-BO**: 42 nm and 175 nm), but domain purities that are not drastically different (**P-EH**: 1.0, **P-BO**: 0.98), suggesting that the decrease in J_{sc} between the two blends is likely due in part to the formation of larger domains that prohibit exciton splitting and charge generation.^{6-8, 43} However, this trend does not hold across the entire series as **P-HD** exhibits smaller domains than **P-BO**. Instead, the large drop in J_{sc} from **P-BO** to **P-HD** may be attributed to the less pure domains in the **P-HD** blend (0.75 vs 0.98). As for the **P-OD** blend, the low J_{sc} can be attributed to a combination of low domain purity (0.63) as well as excessively large domains (47 nm and 128 nm).

Molecular dynamics and bulk-heterojunction organization

MD Simulations. These were performed on isolated polymer chains to understand the interplay of R substituent length and number average molecular mass (M_n) on the conformational space of the present donor polymers and to establish correlations with the experimental BHJ blend morphologies.⁴⁴⁻⁴⁶ Three

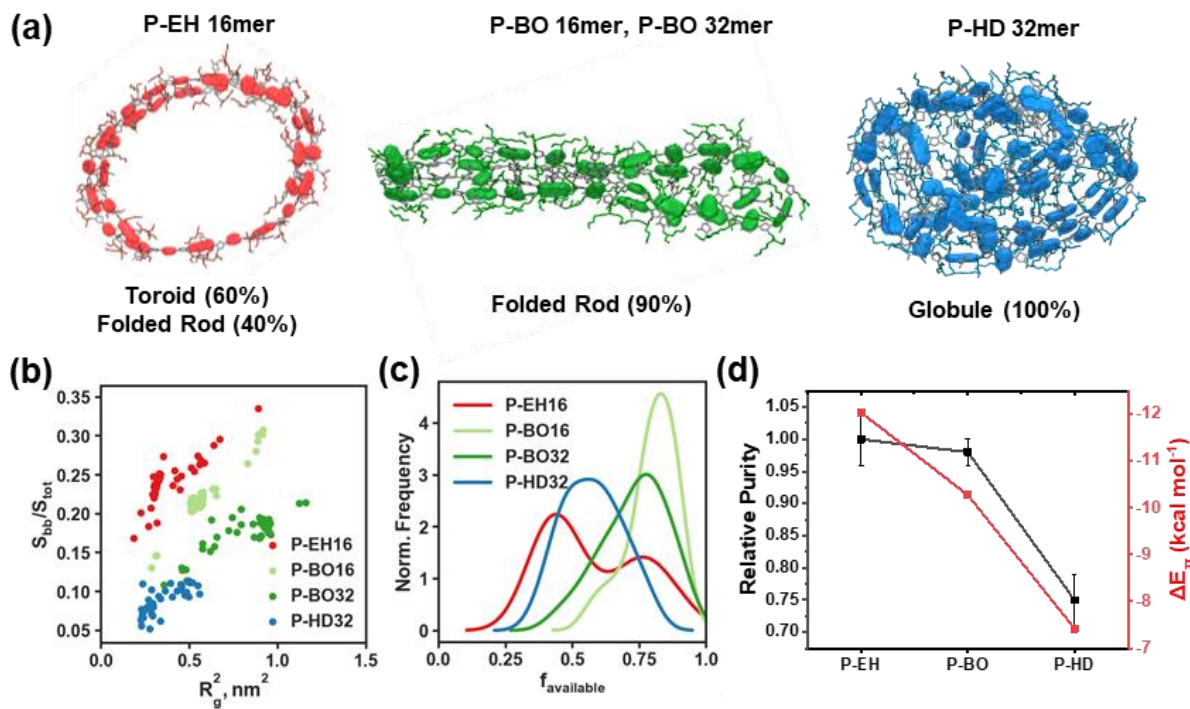


Figure 4. **a)** Graphical representation of chain conformations and available aromatic electronic density, highlighting differences in orientation and order for **P-EH**, (red), **P-BO** (green) and **P-HD** (blue); **b)** SASA of the polymer backbone (S_{bb}), expressed as a fraction of total surface area S_{tot} , as a function of gyration radius R_g^2 ; **c)** Fraction of available aromatic rings for interchain π -interactions; **d)** Black dots: relative domain purities by R-SoXS analysis. Red squares: calculated average energy gain per monomer upon interchain π - π stacking, ΔE_{π} . Note that **P-EH** has two distinct conformations leading to a bimodal distribution, seen in panel **c**. ΔE_{π} calculation for **P-EH** required averaging (by weight) over the two conformations. Dotted lines are a guide to the eye. **Purity error bars in (d) are standard deviation of respective values calculated from R-SoXS data at multiple energies in the range of 283 to 284 eV.**

polymers were considered: **P-EH**, **P-BO** and **P-HD**, each with 16 and 32 repeating units (see “Simulations Setup” in Supplementary for details and Supplementary Figs. 26-41), selected to match the experimental M_n values, where 16 repeat units corresponds to ≈ 18 kg/mol for **P-EH**, and 32 repeat units, ≈ 35 kg/mol, for **P-BO**, **P-HD**, and **P-OD**. Single polymer chains have been shown to indicate melt polymer conformations, especially regarding aspect ratio.^{44, 47} To access folded conformations, simulations used an implicit solvent environment that provides a background dielectric environment similar to that of chlorobenzene used in device fabrication. Polymer conformations obtained from MD were analysed by calculating the following structural descriptors: the end-to-end distance, squared radius of gyration, and persistence length. Additionally, the backbone aromatic group orientational order and their “exposed” surface area available for interchain interactions were calculated (*vide infra*). Representative conformations of each polymer together with their occurrence frequency as a percentage of the total number of simulations performed are shown in Fig. 4a. Generally, polymers having shorter alkyl substituents tend to form ordered conformations in which the backbone rigidity allows little deviation from planarity or folding, whereas more compact, isotropic folding motifs are observed for polymers having longer R groups, corresponding to a higher degree of backbone disorder (Supplementary Figs. 34-36). For **P-EH**, the simulations reveal the prevalence of non-compact toroidal conformations. R group

extension in **P-BO** drives the polymer towards a uniform conformational landscape with almost all MD simulations converging to folded rods with considerable monomer stacking order. Interestingly, the polymer with the longest alkyl substituent, 2-hexyldecyl (**P-HD**) has compact globular conformations without long-range stacking. These results indicate that for **P-EH** the energetic cost of folding is not compensated by stabilising interactions between the conjugated backbone and alkyl substituents, leading to unfolded polymer structures with negligible hairpin kinks. This result contrasts with that of **P-HD**, where due to the large R size, a greater number of stabilising interactions yields more compact folding motifs, disrupting the backbone planarity (π -conjugation). Furthermore, as a control, the conformational order of **P-BO** 16mers was computed and found to exhibit the same conformational order as 32mers, denoting that the balance of different energetic contributions responsible for the conformation stability is governed by the alkyl substituent length rather than by M_n . This finding is corroborated experimentally, which shows that **P-BO** PSCs having different M_n s (18.1 vs. 33.0 kg/mol) perform identically (Supplementary Fig. 25). Importantly, note that this trend agrees with similar observations of coarse-grained polymer chain collapse due to increasing self-interaction energy.⁴⁸

The striking sensitivity of polymer conformation to alkyl substituents, stimulated further MD simulations with a focus

on connecting the observed morphologies with the conformational states. Thus, for each polymer conformation the solvent accessible surface area (SASA) was computed in total (S_{tot}), as well as the SASA attributable to the aromatic backbone (S_{bb}). Additionally, the fraction of “exposed” π -electron density, defined as the fraction of aromatic units having at least one π -MO oriented favorably for inter-chain π - π stacking, was computed (Supplementary Fig. 32a). For each representative **PBTZF4-R** polymer conformation, the “exposed” π -electron density is shown in Fig. 4a. In conjugated polymers, the interplay between intermolecular π - π interactions and intramolecular π -conjugation (backbone stiffness) largely determines whether the polymer crystallizes or forms amorphous aggregates.⁴⁹ To compare the propensity of different polymers to aggregate and/or crystallize, the S_{bb} , normalized by S_{tot} , is shown as a function of the polymer squared radius of gyration R_g^2 (Fig. 4b). The data clearly demonstrate that the more compact polymer chain conformations leads to lower areas of “exposed” conjugated backbone. Interestingly, **P-EH** has a broad distribution of R_g^2 since it forms both extended rods and toroidal conformations, yet both have significant backbone π -electron exposure leading to high S_{bb} .

Bulk-Heterojunction Organization. To translate the SASA-derived π -electron exposure to interchain aggregation propensity, the fraction of available aromatic units per polymer ($f_{available}$) across all conformations was calculated. The criteria determining whether an aromatic site is available or not for interchain π -stacking are based on: 1) the number of intrachain interactions, 2) its orientation with respect to the principal polymer axis (see “Estimation of Available Contacts for Inter-chain π -stacking” in Supplementary for details). The fractions of aromatic units available for interchain π -stacking shown in Fig. 4c. Note that the bulky 2-hexyldecyl substituents constituting >90 % of the corresponding **P-HD** surface area, prevent π - π in-

terchain interactions, thereby reducing the driving force for aggregation and crystallisation. In contrast, the extended, more ordered **P-EH** and **P-BO** conformations with exposed π -conjugated units are more readily available for interchain π - π stacked aggregation. Also, the average energy gain upon interchain π - π interactions, ΔE_{π} , in kcal/mol per interacting unit, was calculated by multiplying the fraction of available contacts (Fig. 4c) by the calculated average stabilisation energy upon **PBTZF4** backbone π - π stacking (Supplementary Fig. 32b). Thus, for **P-EH** and **P-BO**, the higher orientational order results in a far higher driving force for interchain interactions (Fig. 4d) favoring aggregation and ordered domain formation. Note that these data agree with the experimental DSC results (*vide supra*), which show a gradual fall in melting temperature with increasing substituent length, indicating weaker intermolecular interactions.

From the above discussion and generalising the experimental and MD results, we hypothesise that ΔE_{π} , which reflects the driving force for polymer aggregation and crystallization, may be a key factor driving polymer:small molecule blend morphology, hence PCE. ΔE_{π} is found here to correlate strongly with domain purity (Fig. 4d) and is thus a relevant metric correlating polymer conformation with BHJ morphology. For **P-EH**, we hypothesize that the large $|\Delta E_{\pi}|$ and high S_{bb} enable strong aggregation in the solution and prevent **ITIC-Th** infiltration into the donor polymer domains, and upon solvent evaporation, afford high domain purity (Fig. 5). In addition, the low **P-EH** solubility, along with the propensity of the single chains to form ordered aggregates could account for the consistent orientation between the **P-EH** neat and blend films. The opposite situation is concluded for **P-HD** film formation, where pre-aggregation in solution is less favourable due to backbone screening by the large 2-hexyldecyl groups (Fig. 5, low S_{bb} and $|\Delta E_{\pi}|$). We suggest that this low driving force for aggregation and/or crystallisation permits **ITIC-Th** infiltration into polymer

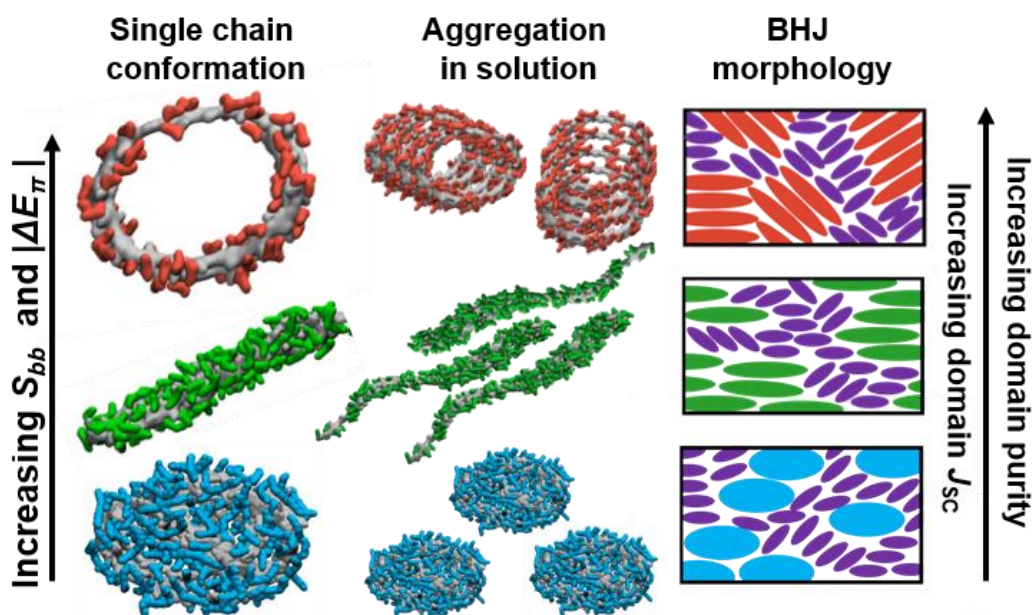


Figure 5. Schematic of polymer conformations affecting aggregation in solution and the resulting film morphology. **Left:** Single polymer chain conformations highlighting the backbone surface area (grey) and that of the alkyl side chains (red: **P-EH**, green: **P-BO**, blue: **P-HD**); **Center:** Polymer nucleation at early stages of film formation. **Right:** resulting solid state BHJ morphologies.

domains, compromising domain purity. Finally, we hypothesize that the more soluble, globular **P-HD** polymer has a lower propensity to template aggregates, allowing domains to organize based on interfacial interactions such as substrate binding, in this case leading to a more π -face-on orientation.⁵⁰ As for **P-BO**, the intermediate $|\Delta E_\pi|$ and S_{bb} results in a driving force for aggregation that leads to a domain purity that is greater than that of **P-HD**, but less than that of **P-EH**. As seen with **P-HD** polymer, the **P-BO** aggregation driving force leads to π -face-on domain orientations form (Fig. 5).^{49, 51}

DISCUSSION & CONCLUSIONS

A **PBTZF4-R** polymer series having alkyl substituents of differing dimensions was synthesized, characterized, and BHJ solar cells with **ITIC-Th** fabricated. Photovoltaic performance data indicate a strong correlation between J_{sc} and FF with blend film morphology and in particular, domain purity, which is dominated by the R group size. The highest PCEs are achieved in blends having the shortest alkyl substituent-containing a polymer, **P-EH** (11.01 %). The higher efficiency stems from more efficient charge generation and collection driven by several factors, including domain purity, domain size, and possibly coincident orientation of the donor and acceptor, although the role of the latter is less well-defined. These findings are in some respects aligned with those of Xia et al²⁷ with a completely different polymer system in which domain purities and PCEs in **R-PBDT2FT:ITIC** BHJ solar cells scale with alkyl substituent size. Interestingly, the same study showed that in blends of the same polymers with a fullerene, J_{sc} values and EQE responses also fall with increasing R group bulk. Nevertheless, the effects of donor polymer alkyl substituent dimensions on morphology are challenging to predict and cannot be predicted solely on the acceptor identity,^{7, 19, 27, 52, 53} suggesting that overall blend morphology reflects a delicate balance of intra/intermolecular forces between components,^{54, 55} and also substituent-dependent polymer backbone conformational order. This agrees with polymer donor:small molecule miscibility studies showing that the crystallinity of both the donor and acceptor are critical to their miscibility,⁵⁶ and highlights the need for a more detailed theoretical understanding of the forces governing BHJ PSC morphology.

To address this gap, alkyl substituent effects on polymer conformations and how these distinct conformations affect blend morphology were investigated via MD simulations. We hypothesize that the larger $|\Delta E_\pi|$ of **P-EH** prevents acceptor infiltration into polymer domains and promotes self-aggregation, affording purer domains and higher crystallinity, whereas polymers containing longer alkyl substituents have a smaller $|\Delta E_\pi|$, affording domains of lower purity and lower crystallinity. From recent work of Ade,¹³ decreasing FF and domain purity resulting from longer alkyl substituents (and decreased $|\Delta E_\pi|$) may be viewed as a fall in the Flory-Huggins interaction parameter (χ) between the two materials. Although ΔE_π does not address thermodynamic mixing as χ does, it does capture the degree of backbone crystallinity and provides a measure of the energetic driving force for domain growth and crystallographic alignment. Given that $|\Delta E_\pi|$ correlates well with measured domain purities and FF s, we envisage that in combination with other computationally derived parameters (including those from the acceptor), ΔE_π can be used to estimate domain

characteristics such as the purity, and crystallinity of a material pair regardless of whether it is under thermodynamic or kinetic control, allowing for rapid, computational evaluation of materials libraries. By including polymer and small molecule conformational details in ΔE_π , a measure of the donor/acceptor interfacial area needed to understand non-radiative voltage losses at the bulk-heterojunction is provided.⁵⁷

Overall, this study not only provides a thorough experimental investigation of the effects of alkyl substituent length tuning on PSC materials, morphological, and photovoltaic parameters but also provides a molecular level understanding, backed by computational results, of why and how these substituents promote different morphologies. $|\Delta E_\pi|$, which reflects the energetic driving force for polymer interchain interaction is a key parameter relating to single chain polymer conformation to BHJ morphology. Such a parameter could be included in semiclassical charge transport device models to account for the role polymer morphology plays in transport rates. More broadly, we believe that the findings presented here, together with further detailed MD morphological studies,⁵⁸ may provide the beginnings of a computationally aided BHJ morphology design.

ASSOCIATED CONTENT

Supporting Information

Methods, along with other experimental details are available in the Supplementary Information. All other data supporting the findings of this study, including donor synthesis and characterizations, photophysics and charge transport, microstructure analysis, femtosecond transient absorption spectroscopy data fitting, test on the **P-BO:ITIC-Th** (low M_n) blend films, and molecular dynamics simulations are available in the Supplementary Information. The data that support the plots within this paper are available from the corresponding authors upon reasonable request.

AUTHOR INFORMATION

Corresponding Author

t-marks@northwestern.edu

a-facchetti@northwestern.edu

f-melkonyan@northwestern.edu

g-schatz@northwestern.edu

kkohlstedt@northwestern.edu

m-wasielewski@northwestern.edu

dean.delongchamp@nist.gov

Author Contributions

The manuscript was written through contributions of all authors. G.W., S.M.S., and M.M contributed equally.

Notes

The authors declare no competing financial interest.

ACKNOWLEDGMENT

Photovoltaic device fabrications & evaluations, spectroscopy and MD simulations were supported by the Center for Light Energy Activated Redox Processes (LEAP) an Energy Frontier Research Center funded by the U.S. Department of Energy, Office of Science, Office of Basic Energy Sciences under Award Number DE-SC0001059 (GW, MM, JLL, WH, TJA, NP-R, JA, RMY, MRW, KLG, GCS, TJM). Synthesis, SCLC device fabrications & evaluations, and R-SoXS were supported by award 70NANB14H012 from U.S. Department of Commerce, National Institute of Standards and Technology as part of the Center for Hierarchical Materials Design (CHiMaD) (GW, SMS, SM, DMD, FSM, TJM). Use of the Advanced Photon Source, an Office of Science User Facility operated for the U.S. Department of Energy (DOE) Office of Science by Argonne National Laboratory, was supported by the U.S. DOE under Contract No. DE-AC02-06CH11357 (JWS, GW). R-SoXS data were acquired at beamline 11.0.1.2 at the Advanced Light Source, which is supported by the Director, Office of Science, Office of Basic Energy Sciences, of the U.S. Department of Energy under contract no. DE-AC02-05CH11231. A.L.D. Kilcoyne and C. Wang of the ALS (DOE) are acknowledged for assisting with the experimental setup and providing instrument maintenance. NEXAFS data were taken on the Soft X-ray Spectroscopy beamline at the Australian Synchrotron, part of ANSTO. This work made use of the EPIC, Keck-II, and/or SPID facilities of Northwestern University's NUANCE Center, which received support from the Soft and Hybrid Nanotechnology Experimental (SHyNE) Resource (NSF NNCI-1542205); the MRSEC program (NSF DMR-1121262) at the Materials Research Center; the International Institute for Nanotechnology (IIN), the Keck Foundation, and the State of Illinois. S.M.S and T.J.A thank the NSF for a Predoctoral Fellowship. S.F. thanks VINNOVA (2015-04859) and the Swedish Research Council (2016-03979) for financial support. The manuscript was written with the contributions of all authors. All authors have given approval to the final version of the manuscript.

REFERENCES

- Lu, L.; Zheng, T.; Wu, Q.; Schneider, A. M.; Zhao, D.; Yu, L., Recent Advances in Bulk Heterojunction Polymer Solar Cells. *Chem. Rev.* **2015**, *115*, (23), 12666-12731.
- Hou, J.; Inganäs, O.; Friend, R. H.; Gao, F., Organic solar cells based on non-fullerene acceptors. *Nat. Mater.* **2018**, *17*, 119.
- Yan, C.; Barlow, S.; Wang, Z.; Yan, H.; Jen, A. K. Y.; Marder, S. R.; Zhan, X., Non-fullerene acceptors for organic solar cells. *Nat. Rev. Mater.* **2018**, *3*, 18003.
- Huang, Y.; Kramer, E. J.; Heeger, A. J.; Bazan, G. C., Bulk Heterojunction Solar Cells: Morphology and Performance Relationships. *Chem. Rev.* **2014**, *114*, (14), 7006-7043.
- Liao, H.-C.; Ho, C.-C.; Chang, C.-Y.; Jao, M.-H.; Darling, S. B.; Su, W.-F., Additives for morphology control in high-efficiency organic solar cells. *Mater. Today* **2013**, *16*, (9), 326-336.
- Li, W.; Hendriks, K. H.; Furlan, A.; Roelofs, W. S. C.; Wienk, M. M.; Janssen, R. A. J., Universal Correlation between Fibril Width and Quantum Efficiency in Diketopyrrolopyrrole-Based Polymer Solar Cells. *J. Am. Chem. Soc.* **2013**, *135*, (50), 18942-18948.
- Li, W.; Hendriks, K. H.; Furlan, A.; Roelofs, W. S. C.; Meskers, S. C. J.; Wienk, M. M.; Janssen, R. A. J., Effect of the Fibrillar Microstructure on the Efficiency of High Molecular Weight Diketopyrrolopyrrole-Based Polymer Solar Cells. *Adv. Mater.* **2014**, *26*, (10), 1565-1570.
- Mukherjee, S.; Proctor, C. M.; Tumbleston, J. R.; Bazan, G. C.; Nguyen, T.-Q.; Ade, H., Importance of Domain Purity and Molecular Packing in Efficient Solution-Processed Small-Molecule Solar Cells. *Adv. Mater.* **2015**, *27*, (6), 1105-1111.
- Huang, W.; Gann, E.; Chandrasekaran, N.; Thomsen, L.; Prasad, S. K. K.; Hodgkiss, J. M.; Kabra, D.; Cheng, Y.-B.; McNeill, C. R., Isolating and quantifying the impact of domain purity on the performance of bulk heterojunction solar cells. *Energy Environ. Sci.* **2017**, *10*, (8), 1843-1853.
- Heintges, G. H. L.; Leenaers, P. J.; Janssen, R. A. J., The effect of side-chain substitution and hot processing on diketopyrrolopyrrole-based polymers for organic solar cells. *J. Mater. Chem. A* **2017**, *5*, (26), 13748-13756.
- Swick, S. M.; Zhu, W.; Matta, M.; Aldrich, T. J.; Harbuzaru, A.; Lopez Navarrete, J. T.; Ponce Ortiz, R.; Kohlstedt, K. L.; Schatz, G. C.; Facchetti, A.; Melkonyan, F. S.; Marks, T. J., Closely packed, low reorganization energy π -extended postfullerene acceptors for efficient polymer solar cells. *Proc. Natl. Acad. Sci. USA* **2018**, *115*, E8341-E8348.
- Aldrich, T. J.; Swick, S. M.; Melkonyan, F. S.; Marks, T. J., Enhancing Indacenodithiophene Acceptor Crystallinity via Substituent Manipulation Increases Organic Solar Cell Efficiency. *Chem. Mater.* **2017**, *29*, (24), 10294-10298.
- Ye, L.; Hu, H.; Ghasemi, M.; Wang, T.; Collins, B. A.; Kim, J.-H.; Jiang, K.; Carpenter, J. H.; Li, H.; Li, Z.; McAfee, T.; Zhao, J.; Chen, X.; Lai, J. L. Y.; Ma, T.; Bredas, J.-L.; Yan, H.; Ade, H., Quantitative relations between interaction parameter, miscibility and function in organic solar cells. *Nat. Mater.* **2018**, *17*, (3), 253-260.
- McDowell, C.; Abdelsamie, M.; Toney, M. F.; Bazan, G. C., Solvent Additives: Key Morphology-Directing Agents for Solution-Processed Organic Solar Cells. *Adv. Mater.* **2018**, *30*, (33), 1707114.
- Fan, B.; Du, X.; Liu, F.; Zhong, W.; Ying, L.; Xie, R.; Tang, X.; An, K.; Xin, J.; Li, N.; Ma, W.; Brabec, C. J.; Huang, F.; Cao, Y., Fine-tuning of the chemical structure of photoactive materials for highly efficient organic photovoltaics. *Nat. Energy* **2018**, *3*, 1051-1058.
- Zhang, Z.-G.; Li, Y., Side-chain engineering of high-efficiency conjugated polymer photovoltaic materials. *Sci. China Chem.* **2015**, *58*, (2), 192-209.
- Min, J.; Luponosov, Y. N.; Gerl, A.; Polinskaya, M. S.; Peregudova, S. M.; Dmitryakov, P. V.; Bakirov, A. V.; Shcherbina, M. A.; Chvalun, S. N.; Grigorian, S.; Kaush-Busies, N.; Ponomarenko, S. A.; Ameri, T.; Brabec, C. J., Alkyl Chain Engineering of Solution-Processable Star-Shaped Molecules for High-Performance Organic Solar Cells. *Adv. Energy Mater.* **2014**, *4*, (5), 1301234.
- Fang, L.; Zhou, Y.; Yao, Y.-X.; Diao, Y.; Lee, W.-Y.; Appleton, A. L.; Allen, R.; Reinspach, J.; Mannsfeld, S. C. B.; Bao, Z., Side-Chain Engineering of Isoindigo-Containing Conjugated Polymers Using Polystyrene for High-Performance Bulk Heterojunction Solar Cells. *Chem. Mater.* **2013**, *25*, (24), 4874-4880.
- Mei, J.; Bao, Z., Side Chain Engineering in Solution-Processable Conjugated Polymers. *Chem. Mater.* **2014**, *26*, (1), 604-615.
- Huang, H.; Bin, H.; Peng, Z.; Qiu, B.; Sun, C.; Liebman-Pelaez, A.; Zhang, Z.-G.; Zhu, C.; Ade, H.; Zhang, Z.; Li, Y., Effect of Side-Chain Engineering of Bithienylbenzodithiophene-alt-fluorobenzotriazole-Based Copolymers on the Thermal Stability and Photovoltaic Performance of Polymer Solar Cells. *Macromolecules* **2018**, *51*, (15), 6028-6036.
- Huo, L.; Xue, X.; Liu, T.; Xiong, W.; Qi, F.; Fan, B.; Xie, D.; Liu, F.; Yang, C.; Sun, Y., Subtle Side-Chain Engineering of Random Terpolymers for High-Performance Organic Solar Cells. *Chem. Mater.* **2018**, *30*, (10), 3294-3300.
- Reid, D. R.; Jackson, N. E.; Bourque, A. J.; Snyder, C. R.; Jones, R. L.; de Pablo, J. J., Aggregation and Solubility of a Model Conjugated Donor-Acceptor Polymer. *J. Phys. Chem. Lett.* **2018**, *9*, (16), 4802-4807.
- Zou, Y.; Wu, Y.; Yang, H.; Dong, Y.; Cui, C.; Li, Y., The effect of alkylthio side chains in oligothiophene-based donor materials for organic solar cells. *Mol. Syst. Des. Eng.* **2018**, *3*, (1), 131-141.
- Huang, W.; Li, M.; Lin, F.; Wu, Y.; Ke, Z.; Zhang, X.; Ma, R.; Yang, T.; Ma, W.; Liang, Y., Rational design of conjugated side chains for high-performance all-polymer solar cells. *Mol. Syst. Des. Eng.* **2018**, *3*, (1), 103-112.
- Timalsina, A.; Hartnett, P. E.; Melkonyan, F. S.; Strzalka, J.;

Table of Contents Graphic

